Supporting Information

Immiscible phase-separation electrolyte and interface ion transfer

electrochemistry enable zinc/lithium hybrid batteries with 3.5 V-class operating

voltage

Ao Chen[a], Yaqin Zhang[a], Qing Li[a], Guojing Liang[a], Shuo Yang[a], Zhaodong Huang[b],

Qi Yang[b], Hong Hu[a], Xinliang Li[a], Ze Chen[a], Jun Fan[a*], Chunyi Zhi[a,b,c,d,e*]

[a] Department of Materials Science and Engineering, City University of Hong Kong, 83 Tat Chee Avenue, Kowloon, Hong Kong, China

[b] Hong Kong Center for Cerebro-Cardiovascular Health Engineering (COCHE), Shatin, NT, HKSAR, China

[c] Centre for Advanced Nuclear Safety and Sustainable Development, City University of Hong Kong, 83 Tat Chee Avenue, Kowloon, Hong Kong, 999077, China

[d] Hong Kong Institute for Clean Energy, City University of Hong Kong, Kowloon 999077, Hong Kong

[e] Hong Kong Institute for Advanced Study, City University of Hong Kong, Kowloon, Hong Kong, 999077, China

Materials and Methods

Materials: N-methyl-N-butylpyrrolidinium bis(trifluoromethylsulfonyl)imide (Py$_{14}$TFSI, 98%), 1,1,2,2-Tetrafluoroethyl 2,2,3,3-Tetrafluoropropyl Ether (HFE, 98%) Bis(trifluoromethane)sulfonimide lithium salt (LiTFSI, 99%), Lithium hydroxide, anhydrous (LiOH, 99.9%), Sodium hydroxide (NaOH, 98%), Zinc oxide (ZnO, 99.8%), Cobalt chloride hexahydrate (CoCl$_2$·6H$_2$O), Manganese Chloride Tetrahydrate (MnCl$_2$·4H$_2$O), Urea (99.95%), Lithium carbonate (Li$_2$CO$_3$, 99%), Polyvinylpyrrolidone (PVP, M.W. $\sim$ 40,000, K30), Ascorbic acid (99%) was purchased from Aladdin. Poly(vinyl alcohol) (PVA, M.W. $\sim$ 100,000) was purchased from UNI-CHEM and used as received.

Preparation of electrolytes. Oil-phase organic electrolyte was prepared by dissolving 1 M LiTFSI (mol-salt in kg-solvent) in Py$_{14}$TFSI at 100 °C, and then mixed with HFE at the volume ratio of 1:1. Aqueous electrolyte was prepared by dissolving 3 M LiOH, 0.3 M ZnO and 2 M LiTFSI in DI water. 50 wt% NaOH solution with saturated LiTFSI was employed as the concentrated alkali electrolyte. Alkaline gel electrolyte was fabricated by a typical method. 30 wt% PVA was dissolved in the aqueous electrolyte at 95°C, and the gel electrolyte could be obtained after cooling.

Preparation of cathode materials. Commercial LiFePO$_4$, LiMn$_2$O$_4$ and LiNi$_{0.5}$Mn$_{1.5}$O$_4$ were purchased from Guangdong Canrd New Energy Technology Co.,Ltd. LiCoMnO$_4$ was synthesized following a previously reported procedure.[1] In a typical run, 500 mg CoCl$_2$·6H$_2$O and 347 mg MnCl$_2$·4H$_2$O were dissolved in 66 ml DI water, and then 2 g PVP, 2.46 g urea and 2.5 g ascorbic acid were added to the solution.

After stirring for 1 h, the solution was transferred to 100 ml Teflon-lined stainless-steel autoclave and maintained at 160 °C for 6 h. Subsequently, the solution was centrifuged and washed with DI water, and then dried at 60 °C for 12 h. The obtained $CoMnCO_3$ was first calcinated at 400 °C for 5 h in air. Finally, the $LiCoMnO_4$ could be obtained by calcinating the mixture of 700 mg $CoMnO_X$ and 165 mg Li_2CO_3 at 800 °C for 24 h in O_2 environment.

Materials characterizations. The X-Ray Diffraction (XRD) was performed on a Bruker D2 Phaser. The electrodes at different stages were employed for the ex-situ measurements. Scanning electron microscopy (SEM) was taken by FEI/Philips XL3. Raman spectra were tested with PerkinElmer Raman 400F Spectrometer using a 532 nm diode-pumped solid-state laser. The electrolyte was load in a quartz capillary tube.

Electrochemical measurements. The cathode electrode was prepared by mixing active materials, Super P and polyvinylidene fluoride (PVDF) at weight ratio of 8:1:1 in Nmethylpyrrolidinone (NMP), and the slurry was then coated on an Al foil and dried at 70 °C in vacuum for 12 h. The cell was assembled by using a customized device (**Supplementary Fig.1**). First, the cathode electrode was in the bottom of device. Then the oil-phase organic electrolyte and aqueous electrolyte was added. Due to the immiscibility, the oil-phase organic electrolyte and aqueous electrolyte automatically form phase separation electrolyte. Zn foil as the anode was placed in the aqueous electrolyte. For the ZnO anode, ZnO and PVDF was mixed at weight ratio of 9:1 in NMP and the slurry was then coated on Zn foil. The electrode was dried at 60 °C in vacuum for 12 h.

For the thin soft packed zinc battery, the fabrication is similar with fabrication of the conventional pouch cells. Alkaline gel was coated on the anode and then the customized porous polypropylene (pp) separator was placed between alkaline gel and cathode. The cell was sealed with package film and injected oil-phase organic electrolyte. The Li‖LiMn$_2$O$_4$ batteries were assembled in a pure argon filled dry glove box (H$_2$O, O$_2$ < 0.5 ppm) by using oil-phase organic electrolyte, Celgard 2325 as the separator and lithium foil as the anode. The galvanostatic discharge-charge tests were conducted on Land BT2000 battery test system. Cyclic voltammetry (CV) and linear sweep voltammetry (LSV) was carried out using CHI 760E electrochemical workstation. EIS measurement was performed with a 5 mV amplitude AC signal with frequency ranging from 100 kHz to 0.1 Hz. The ion transfer potential was tested by using a four-electrode configuration. Typically, the Hg/HgO and Ag/AgCl were placed in aqueous and oil-phase organic electrolytes, respectively, as the reference electrodes. Ti foil was employed as the work electrodes.

Simulation Details

The structures of all cations, anions, and molecules were optimized using the Gaussian 09 software package at the B3LYP/6-311G(d,p) level of theory,[2,3] and the optimized geometries at local minima or global minima were ensured by the absence of imaginary vibrational frequency. The solvation free energies for lithium and zinc ions were calculated by designing thermodynamic cycles.[4] Then, the single-conformation two-stage restraint electrostatic potentials (RESP) method developed by Bayly et al. was used to obtain the atomic charges by fitting the electrostatic potential

calculated at the same level.[5,6] Molecular dynamics simulations were carried out for bulk systems (S1-S4) and interfacial systems (S5, S6) in Table 1. The reported OPLS-AA force field was applied for ions and molecules, and SPCE model was used for water in our simulation.[7] The initial simulation box was prepared by PACKMOL in a periodic boundary condition (PBC) box in three directions, and the energy minimization was performed with the steepest descent method to remove the possible coordinate collision of the configurations. Next, the system was equilibrated for 2 ns under the NVT ensemble at 500 K by Velocity Rescaling,[8] followed by a 4 ns simulation under NPT ensemble at 298 K and 1 bar using the Parrinello−Rahman algorithm.[9] For bulk systems, the production simulation continued under the NPT ensemble to run for an additional 20 ns to collect the data for analyzing the structures. For the calculation of long-range electrostatics interactions, particle-mesh Ewald summation was used,[10] and the cutoff radius for electrostatics and vdW interaction was 1.2 nm. All covalent bonds containing hydrogen were fixed using the LINCS algorithm.[11] Radial distribution function (RDF) and coordination numbers were analyzed based on total 20 ns trajectories. For the interfacial systems, the individual bulk boxes were built together along the z direction with the water phase in the middle and two oil phases in both sides. Then, to ensure the full equilibrium, the interface boxes were equilibrated for 10 ns under NPT ensemble until no apparent deviation for the number density profiles. Afterwards, the data was collected by 20 ns NVT production run without and with electric field (102400 V m^{-1}).

Table 1. Compositions of the simulated systems. S1: Zn(TFSI)$_2$ 0.2 M,LiTFSI 0.4 M

in $Py_{14}TFSI$-HFE; S2: $Zn(TFSI)_2$ 0.2 M, LiTFSI 0.4 M in water; S3: $Zn(OTF)_2$ 0.2 M, LiTFSI 0.4 M in water; S4: $Zn(OTF)_2$ 1 M, LiTFSI 21 M in water; S5: without electric field; S6: with electric field 102400 V m^{-1}.

	Systems	Li$^+$	Zn^{2+}	TFSI$^-$	OTF$^-$	Pyr$^+$	HFE	H$_2$O	OH$^-$
S1		40	20	280		200	300		
S2		40	20	80				5550	
S3		40	20	40	40			5550	
S4		2100	100	2100	200			5550	
S5	Aqueous phase	500	30	200				5550	420
	Oil phase	50		250		200	300		
S6	Aqueous phase	500	30	200				5550	420
	Oil phase	50		250		200	300		

3 M LiOH/ 0.3 M ZnO/ 2 M LiTFSI in water

0.5 M LiTFSI in Py$_{14}$TFSI-HFE

PSE

Zn foil
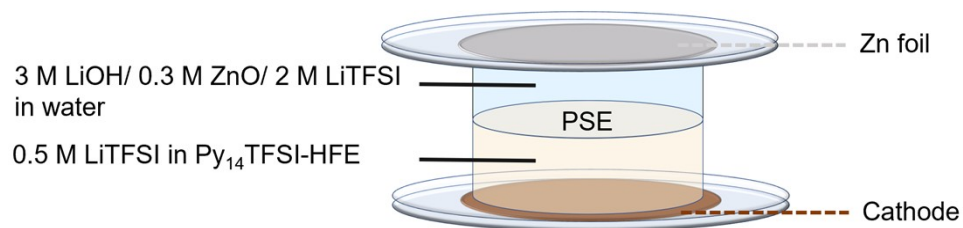
Cathode

Supplementary Fig.1| Schematic illustration of the customized zinc-based hybrid battery with the PSE. The cathode was put at the bottom of the quartz flange and the zinc anode was immersed in the aqueous electrolyte.
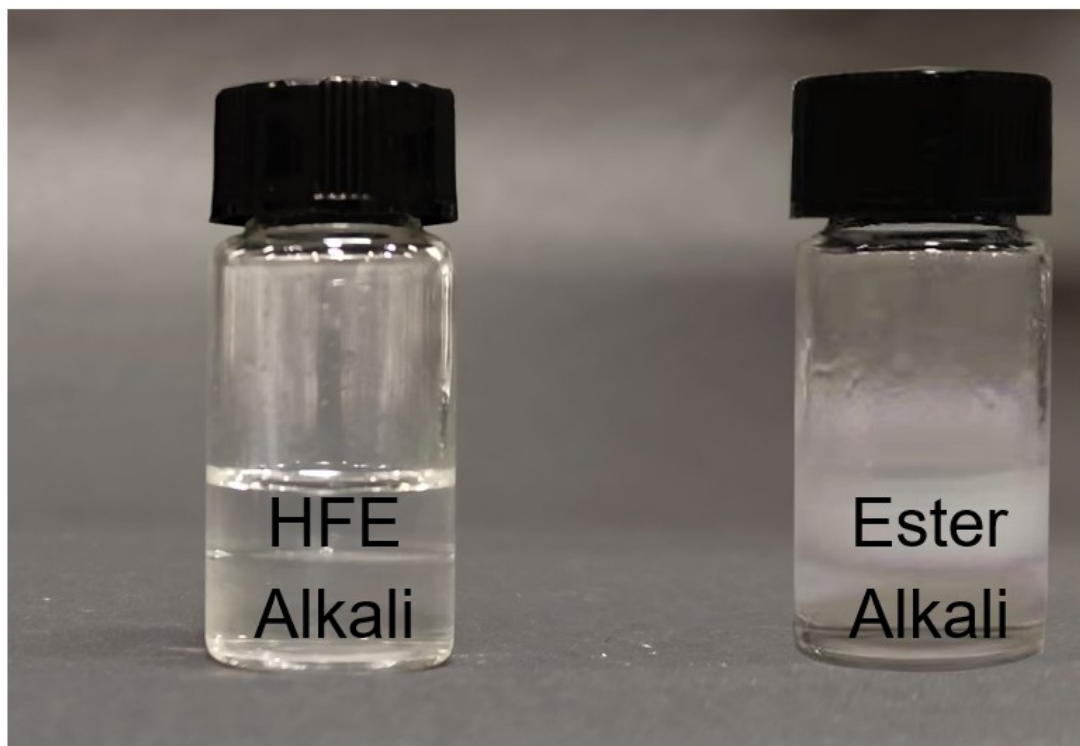
Supplementary Fig.2| Stability comparison. The high stability of HFE against alkali and obvious hydrolyzation of ester solvent.
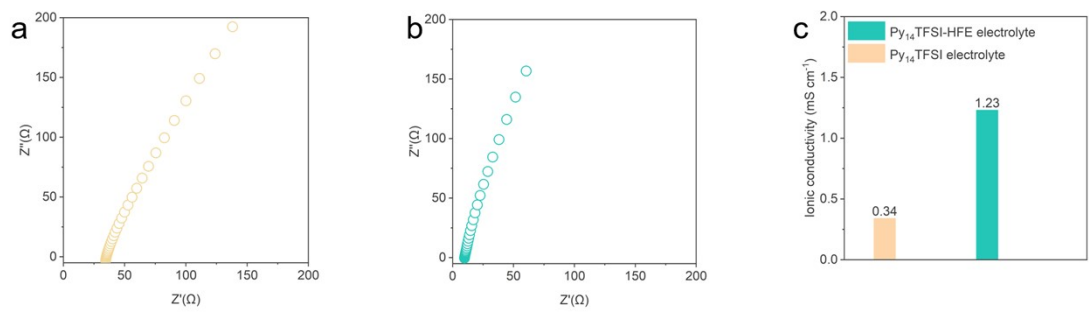
Supplementary Fig.3| Comparison of ionic conductivities. (a) Nyquist plot of Py$_{14}$TFSI electrolyte at room temperature. (b) Nyquist plot of Py$_{14}$TFSI-HFE electrolyte at room temperature. (c) Ionic conductivity of Py$_{14}$TFSI and Py$_{14}$TFSI-HFE electrolytes, respectively.
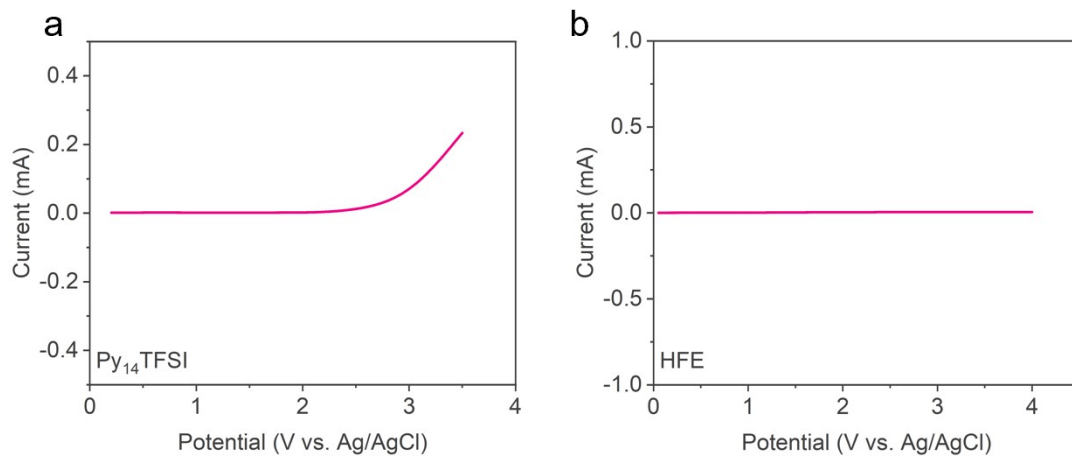
Supplementary Fig.4| The cathodic electrochemical stability window of Py$_{14}$TFSI and HFE. (a) The cathodic stability window of Py$_{14}$TFSI. (b) The cathodic stability window of HFE and no obvious decomposition can be observed for HFE up to 4 V. Measurements were taken with linear sweep voltammetry on Ti electrodes at a scan rate of 5 mV s^{-1}.
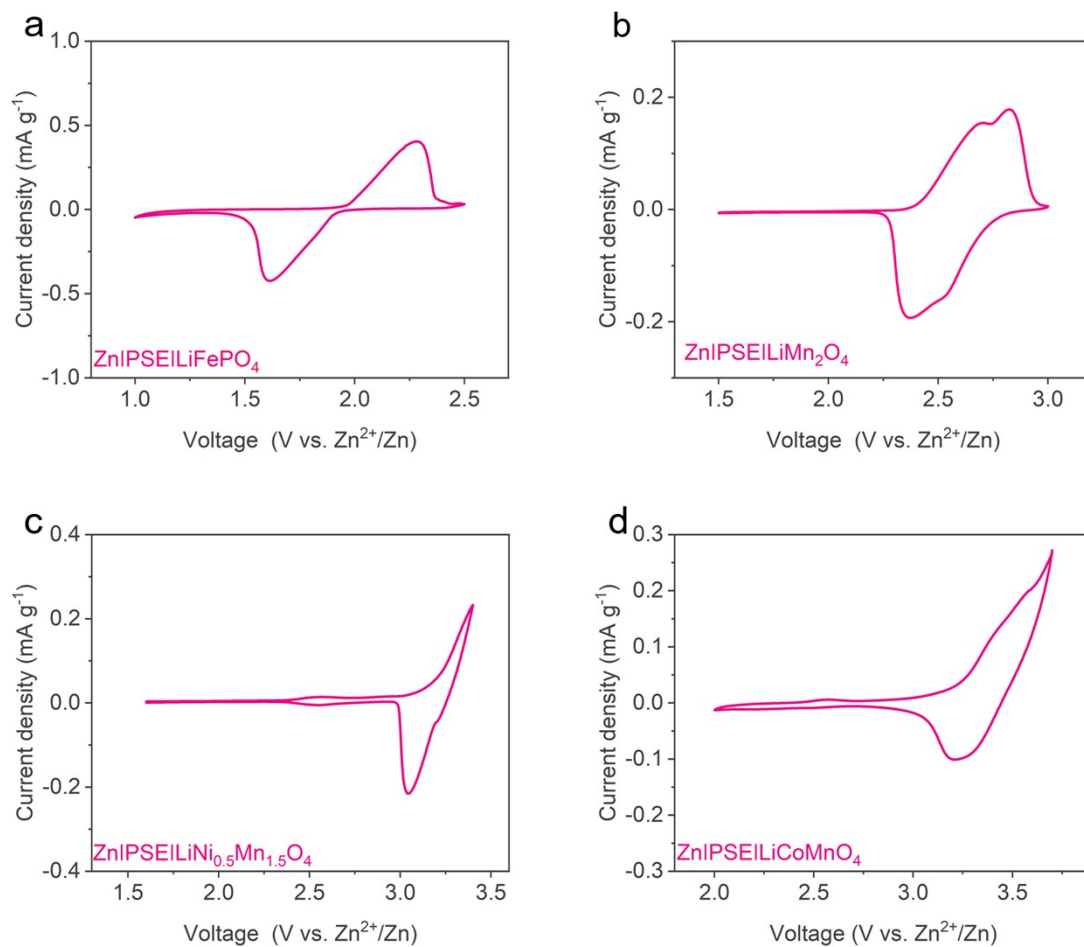
Supplementary Fig.5| (a-d) CV of the Zn|PSE|LiFePO$_4$, Zn|PSE|LiMn$_2$O$_4$, Zn|PSE|LiNi$_{0.5}$Mn$_{1.5}$O$_4$ and Zn|PSE|LiCoMnO$_4$ batteries. The CV was conducted at a scanning rate of 0.1 mV s^{-1}.
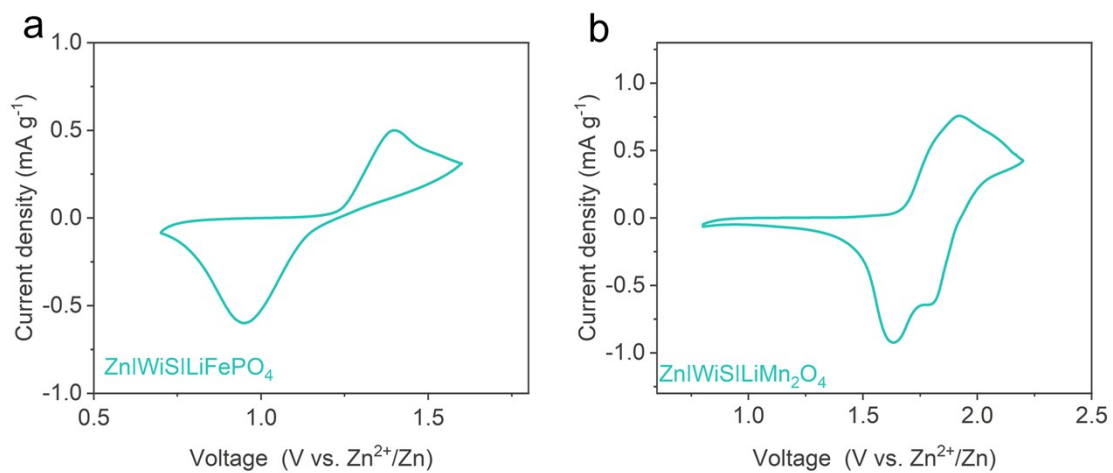
Supplementary Fig.6| (a) The CV of the Zn|WiS|LiFePO$_4$ battery. (b) The CV of the Zn|WiS|LiMn$_2$O$_4$ battery. The CV was measured at a scanning rate of 0.3 mV s^{-1}.
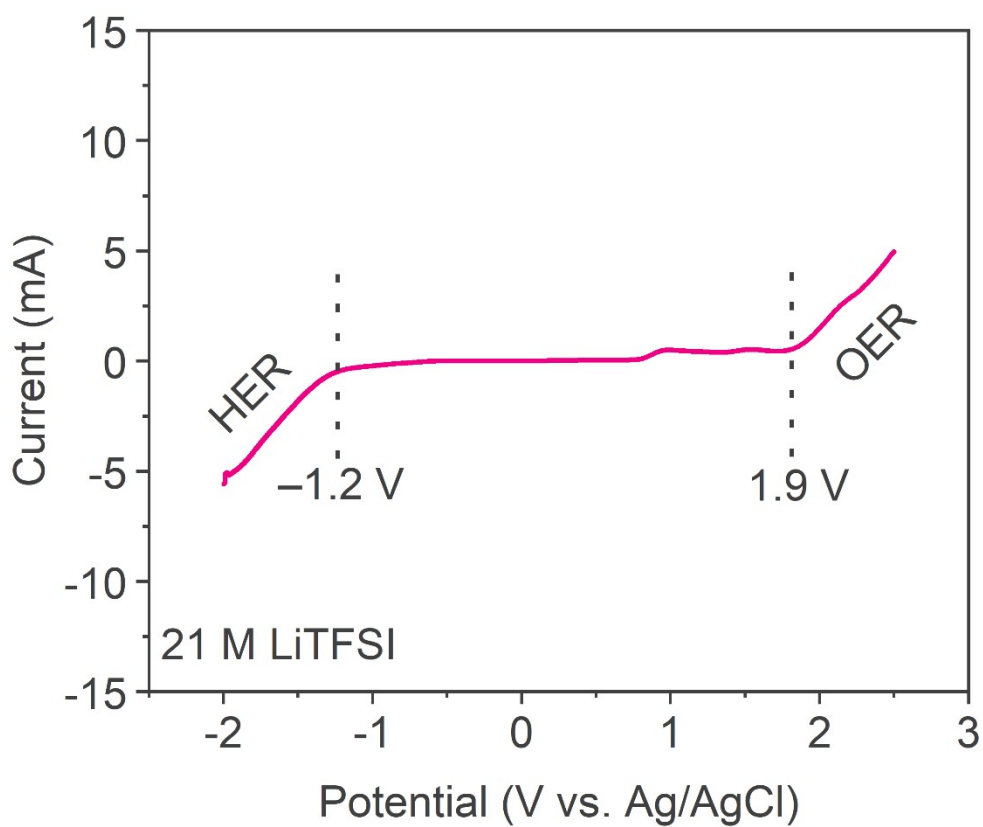
Supplementary Fig.7| Electrochemical stability window of the WiS electrolyte. Measurements were taken with CV on Ti working electrodes between –2 V and 2.5 V versus Ag/AgCl at 5 mV s^{-1}.
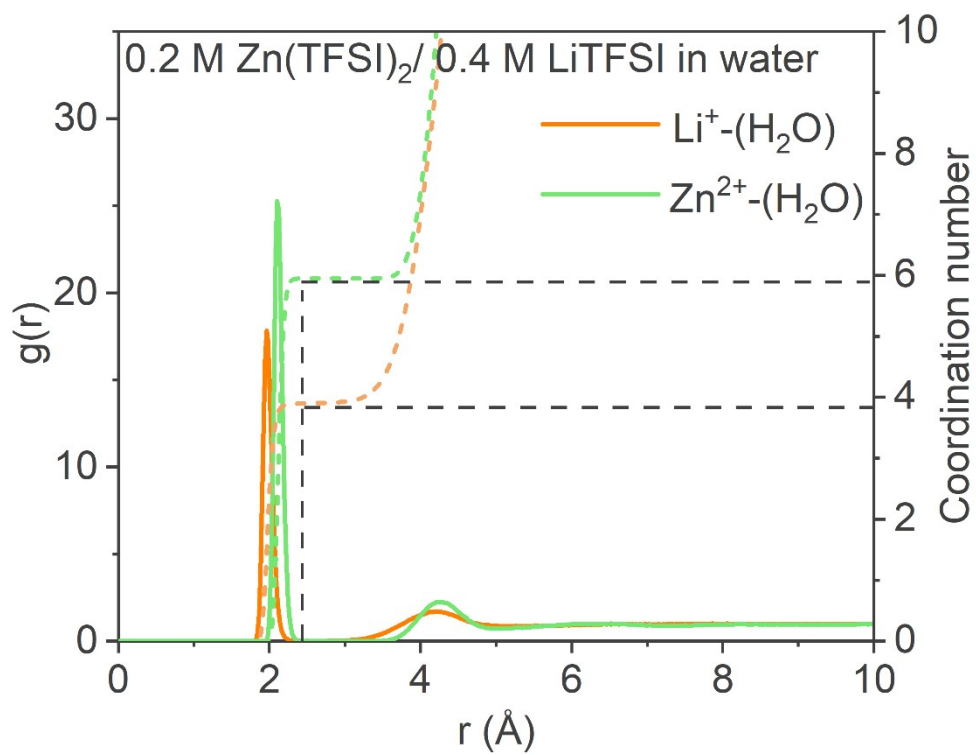
Supplementary Fig.8| Radial distribution functions of $Li^+–(H_2O)$ and $Zn^{2+}–(H_2O)$ pairs in 0.2 M $Zn(TFSI)_2$/ 0.4 M LiTFSI dissolved aqueous electrolyte.

Supplementary Note 1

XRD patterns of LiFePO$_4$ during charge-discharge process also demonstrates the typical phase transformation, which is also in consistent with the changes of LiFePO$_4$ in conventional lithium salt based organic electrolyte (**Supplementary Fig.9**).[12-14] During charging, the (200), (211) and (311) peaks quickly shift to higher scattering angles, indicating emergence of the FePO$_4$ phase. The reverse behavior could be observed in discharging process. Peaks of the FePO$_4$ phase return to lower scattering angles and the LiFePO$_4$ phase reappear with the lithiation of FePO$_4$. The LiNi$_{0.5}$Mn$_{1.5}$O$_4$ and LiCoMnO$_4$ cathodes also exhibited the same reversible phase transformation in the PSE as in the conventional organic electrolytes (**Supplementary Fig.10 and 11**).[15-19] Therefore, through the immiscible design of the PSE, the Zn^{2+} is confined in the aqueous electrolyte by the strong coordination effect, which allows the cathode materials to be cycled.
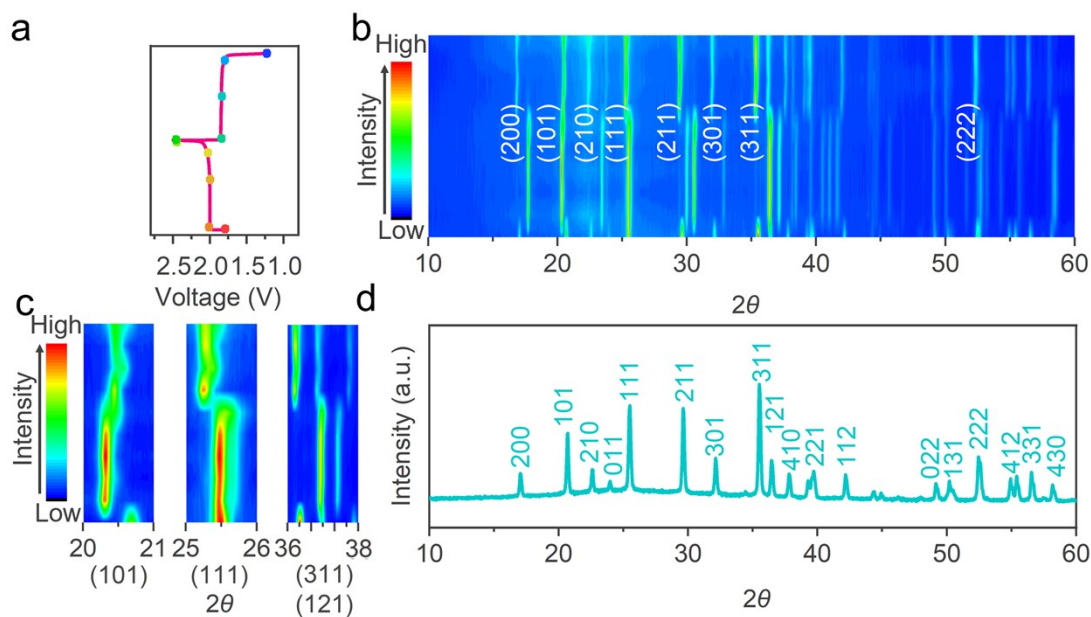
Supplementary Fig.9| Ex-situ XRD patterns of LiFePO₄ were collected between 1.2 and 2.5 V during charge-discharge and the selected points for ex-situ XRD patterns of LiFePO₄. (a) Charge-discharge profile of the Zn|PSE|LiFePO₄ battery. XRD patterns were collected from the electrodes at various charge and discharge states. (b) The contour plot of the corresponding XRD patterns. (c) Contour plots of the selected typical peaks of (101), (111), (311) and (121). (d) XRD pattern of initial LiFeO₄ power. The Bragg peaks ranged from 10 and 60° exhibit shift during the charge-discharge process, which is consistent with the changes of LiFePO₄ in conventional lithium salt dissolved organic electrolyte. The result demonstrates that Li⁺ ions are the charge carriers in the PSE.
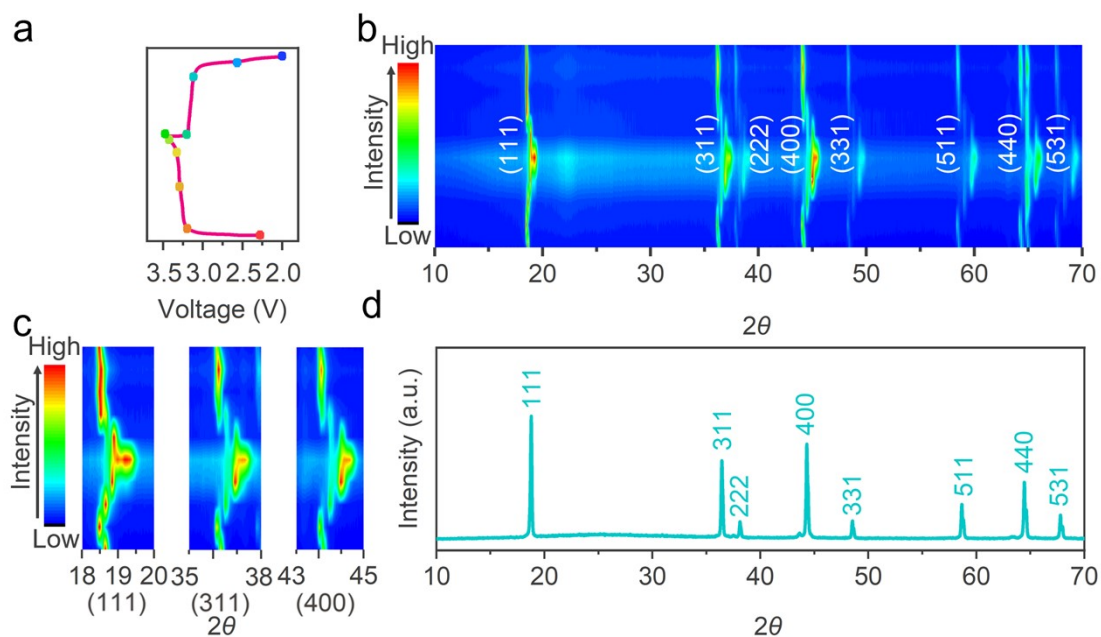
Supplementary Fig.10| Ex-situ XRD patterns of LiNi$_{0.5}$Mn$_{1.5}$O$_4$ were collected between 2.0 and 3.45 V during charge-discharge process. (a) The charge-discharge profile of Zn|PSE|LiNi$_{0.5}$Mn$_{1.5}$O$_4$ battery. XRD patterns were collected from the electrodes at various charge and discharge states. (b) Contour plot of the corresponding XRD patterns. (c) Contour plots of selected typical peaks of (111), (311) and (400). (d) XRD pattern of initial LiNi$_{0.5}$Mn$_{1.5}$O$_4$ power. LiNi$_{0.5}$Mn$_{1.5}$O$_4$ exhibits the typical peaks of (111), (311) and (400) broaden during charging process and recover to its initial state after complete discharge.
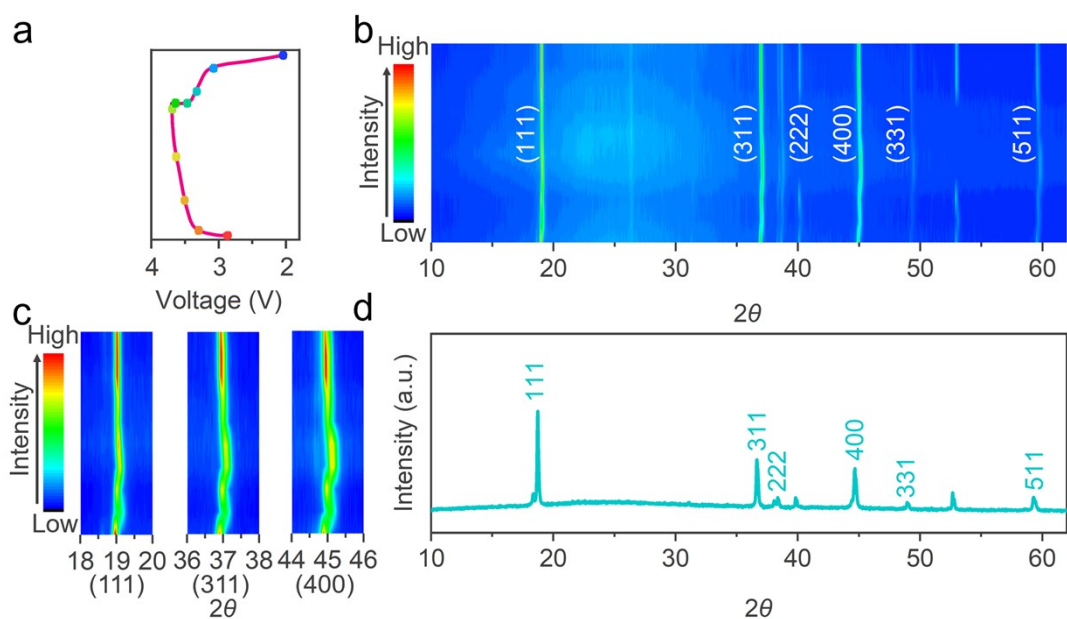
Supplementary Fig.11| Ex-situ XRD patterns of LiCoMnO$_4$ were collected between 2.0 and 3.7 V during charge-discharge process. (a) Charge-discharge profile of Zn|PSE|LiCoMnO$_4$ battery. XRD patterns were collected from the electrodes at various charge and discharge states. (b) Contour plot of the corresponding XRD patterns. (c) Contour plots of selected typical peaks of (111), (311) and (400). (d)   XRD pattern of initial LiNi$_{0.5}$Mn$_{1.5}$O$_4$ power. The Bragg peaks ranged from 10 $^\circ$ and 60 $^\circ$ exhibits continuous shift during the charge-discharge process. However, due to the slight change of the size of Co from Co^{3+} to Co^{4+}, no obvious broadening can be observed during the charge and discharge.[1] The results are consistent with the features of LiCoMnO$_4$ in the Li||LiCoMnO$_4$ batteries.
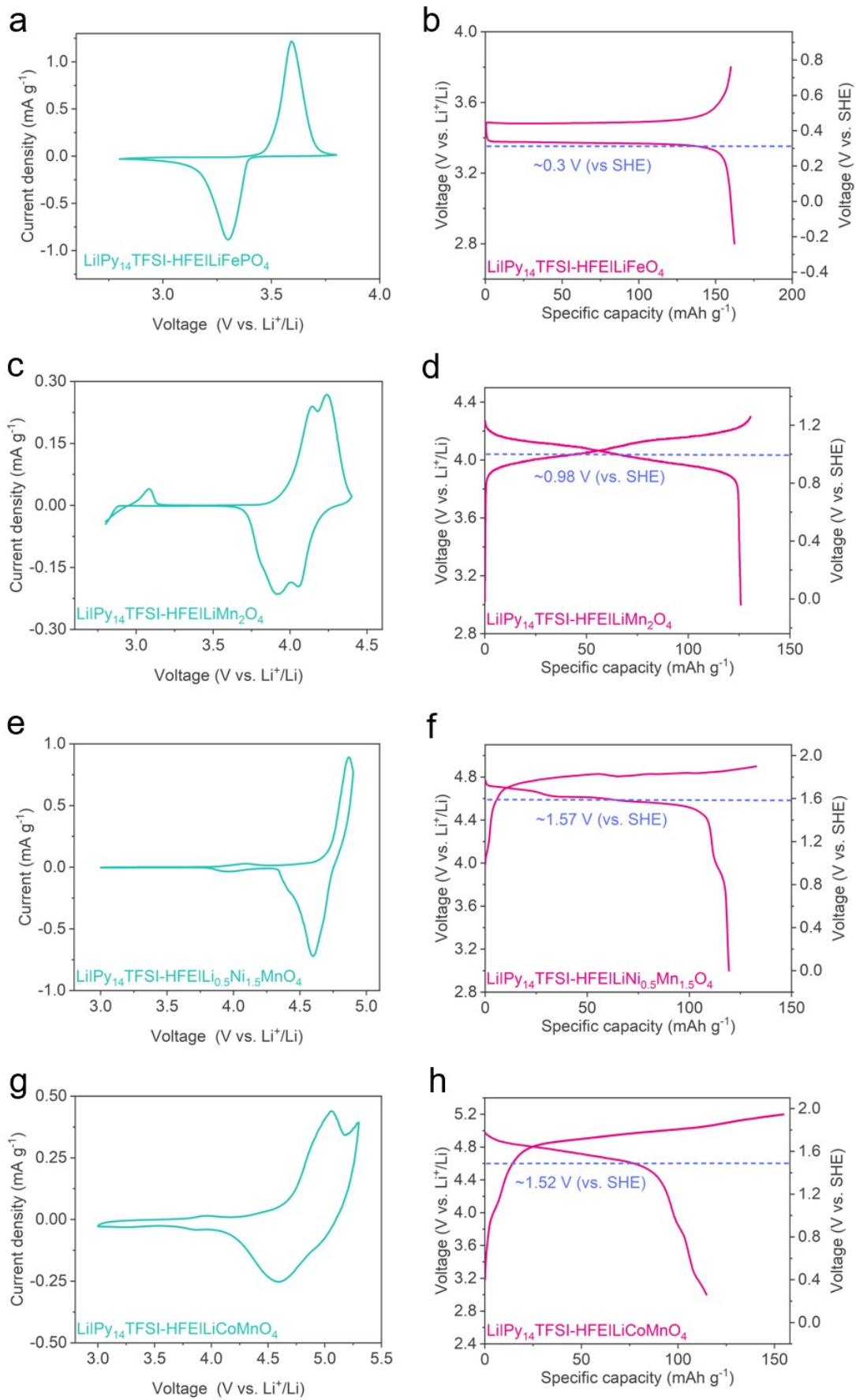
Supplementary Fig.12| (a-h) CVs and corresponding charge-discharge profiles of

LiFePO$_4$, LiMn$_2$O$_4$, LiNi$_{0.5}$Mn$_{1.5}$O$_4$ and LiCoMnO$_4$ in the Py$_{14}$TFSI-HFE electrolyte. The cyclic voltammetry was conducted at a scanning rate of 0.3 mV s^{-1} and the discharge current density is 0.2 C.
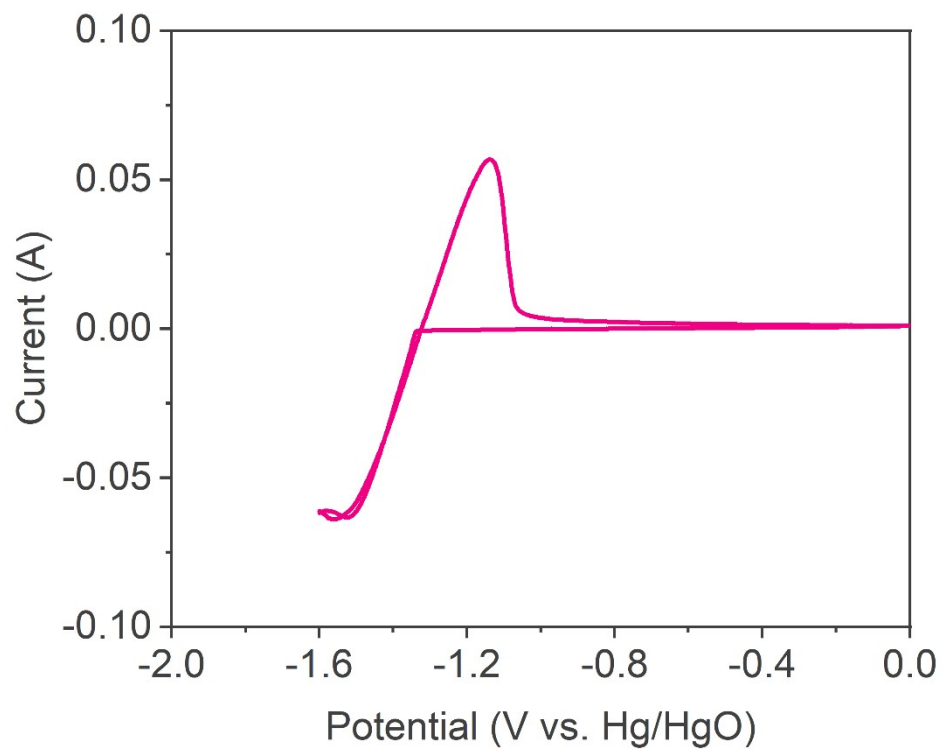
Supplementary Fig.13| CV curve of Zn/Zn(OH)$_4^{2-}$ redox pairs. Zn^{2+} was plated and stripped at -1.33 V (vs. Hg/HgO). Measurement was taken with CV at a scan rate of 5 mV s^{-1}.
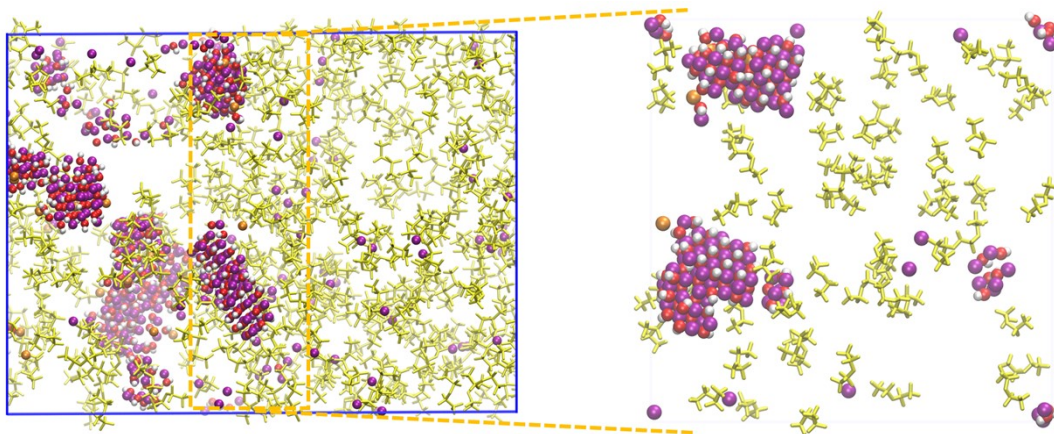
Supplementary Fig.14| Snapshot of the cross section of liquid-liquid interface in PSE at static state. Purple ball: Li$^+$, Orange ball: Zn^{2+}, Red and white ball: OH$^-$, Yellow: TFSI$^-$.
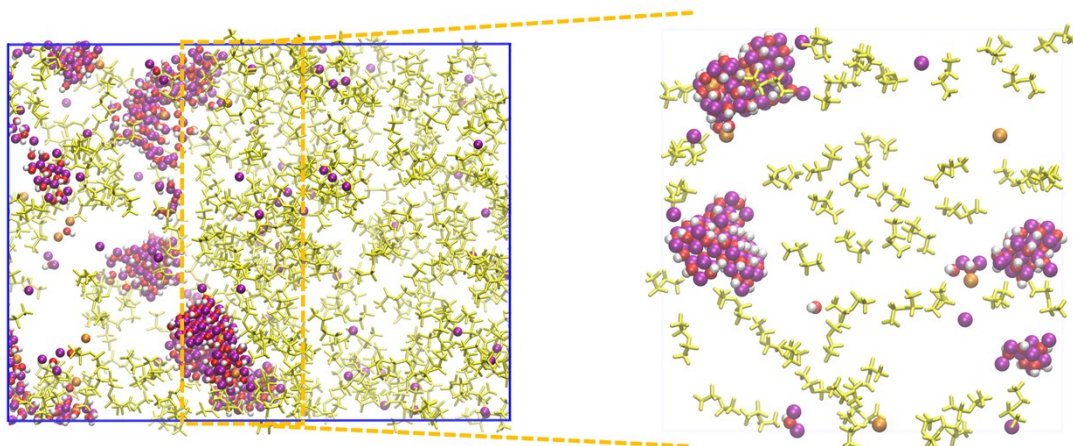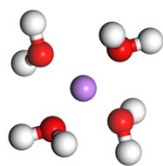
Supplementary Fig.15| Snapshot of the cross section of liquid-liquid interface in PSE during discharging. Purple ball: Li$^+$, Orange ball: Zn^{2+}, Red and white ball: OH$^-$, Yellow: TFSI$^-$.
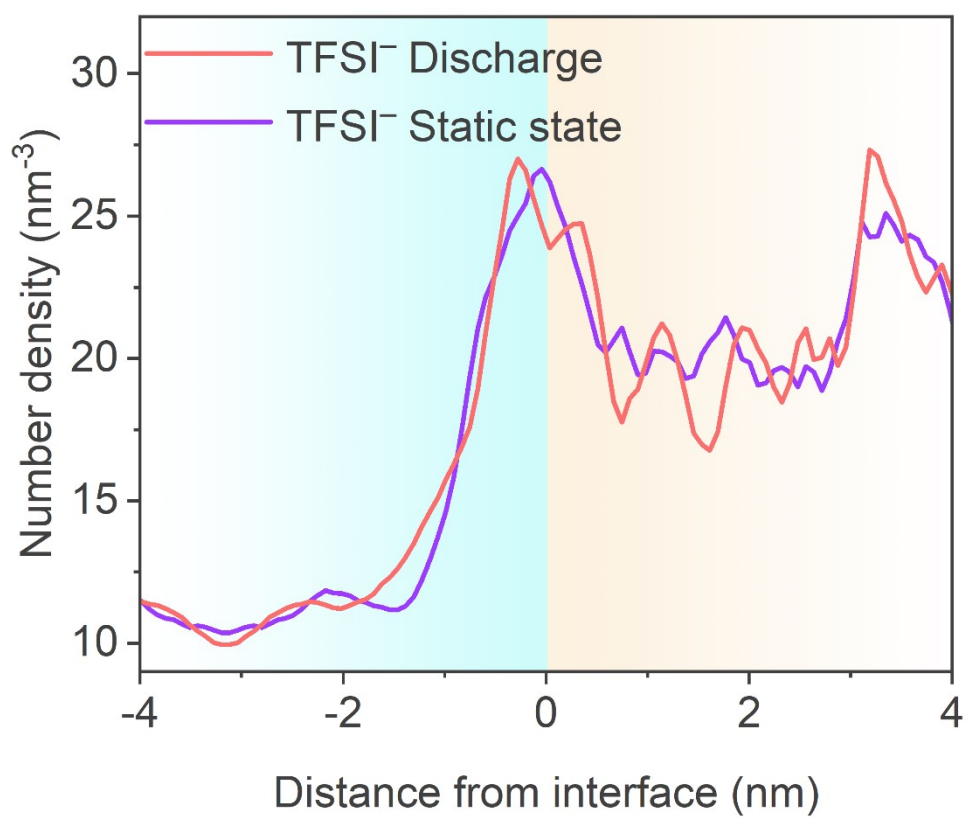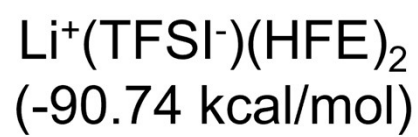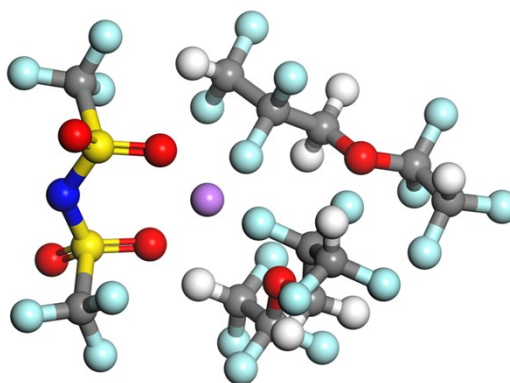
Supplementary Fig.16| Comparison of the number density of TFSI$^-$ ions at the liquid-liquid interface in PSE at static and discharging state.

a

b

Li$^+$(H$_2$O)$_4$
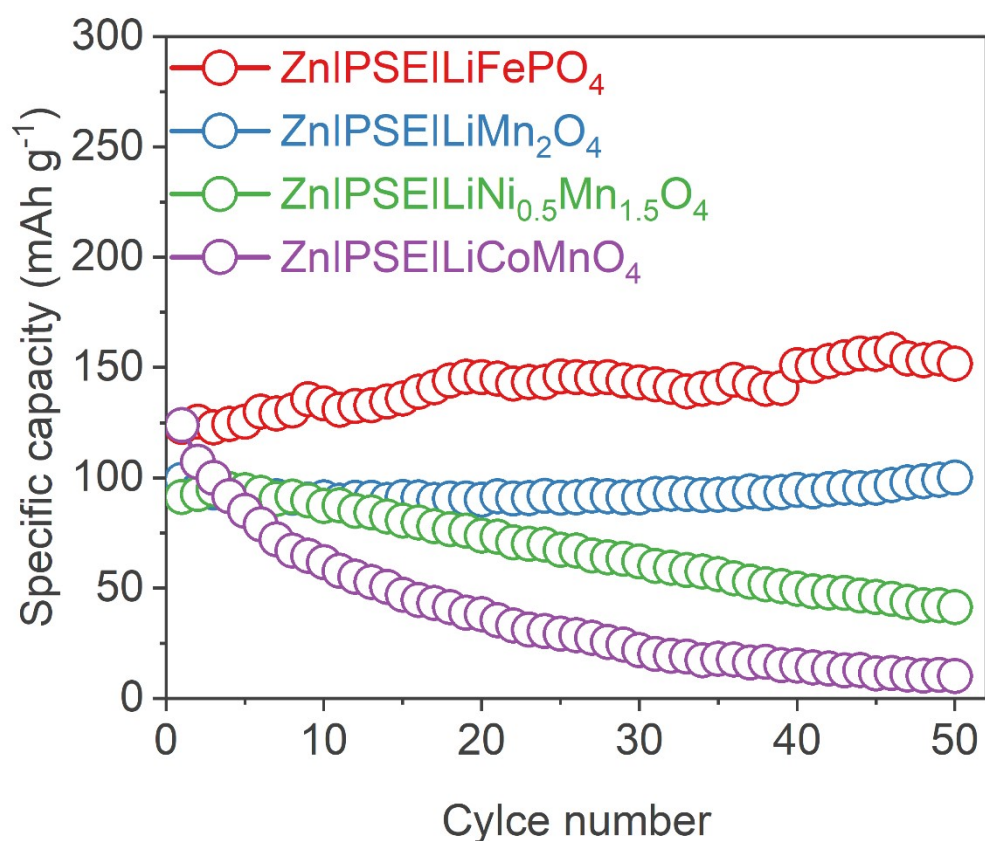(-114.37 kcal/mol)

Li$^+$(TFSI$^-$)(HFE)$_2$
(-90.74 kcal/mol)
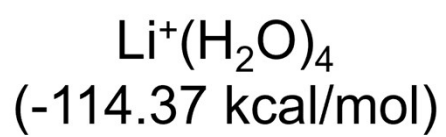
Supplementary Fig.17| The solvation structure and corresponding solvation energy of

Li$^+$ in (a) aqueous electrolyte and (b) oil-phase electrolyte.

Supplementary Fig.18| The cyclic performances of $Zn|PSE|LiFePO_4$, $Zn|PSE|LiMn_2O_4$, $Zn|PSE|LiNi_{0.5}Mn_{1.5}O_4$ and $Zn|PSE|LiCoMnO_4$ batteries at 1C. Compared with the $LiNi_{0.5}Mn_{1.5}O_4$ and the $LiCoMnO_4$, the commercialized $LiFePO_4$ and $LiMn_2O_4$ exhibit better cycling stability. This is because the $LiNi_{0.5}Mn_{1.5}O_4$ and $LiCoMnO_4$ materials usually need coating or additives in the electrolyte to form stable cathode electrolyte interface.
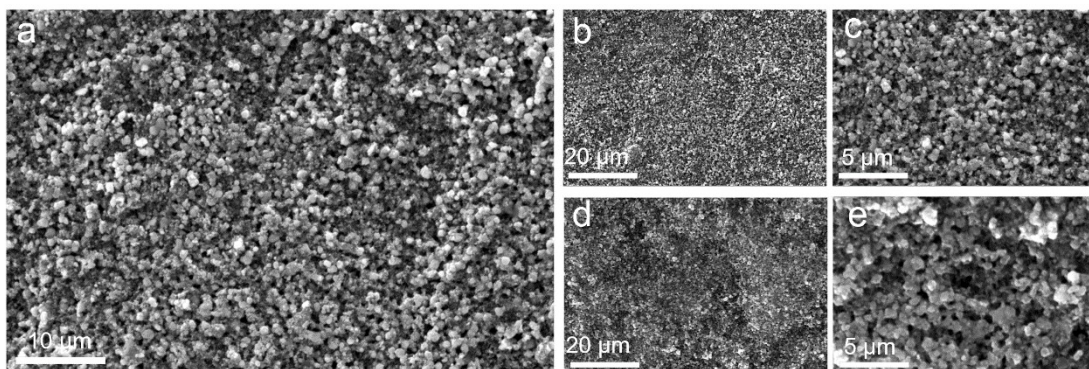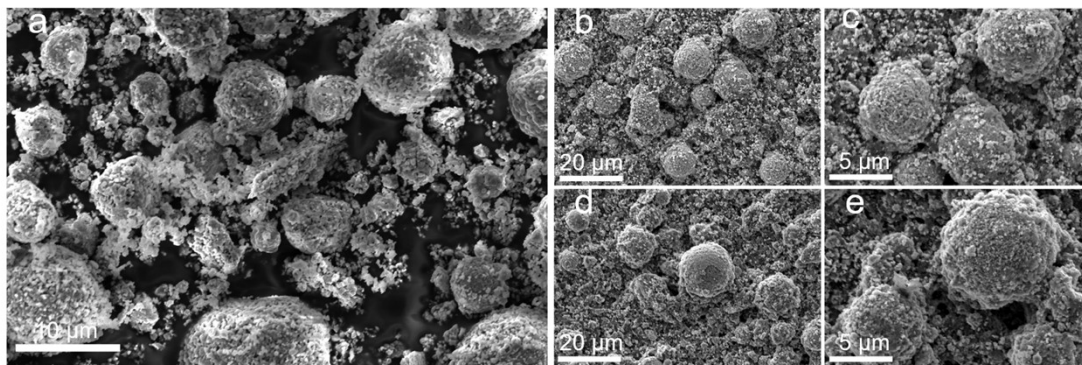
Supplementary Fig.19| Scanning electron microscope images of electrode materials. (a) SEM images of commercial LiFePO$_4$ material. (b-c) SEM images of LiFePO$_4$ cathode before cycling. (d-e) Images of LiFePO$_4$ cathode after 50 cycles at 1 C for Zn|PSE|LiFePO$_4$ battery.
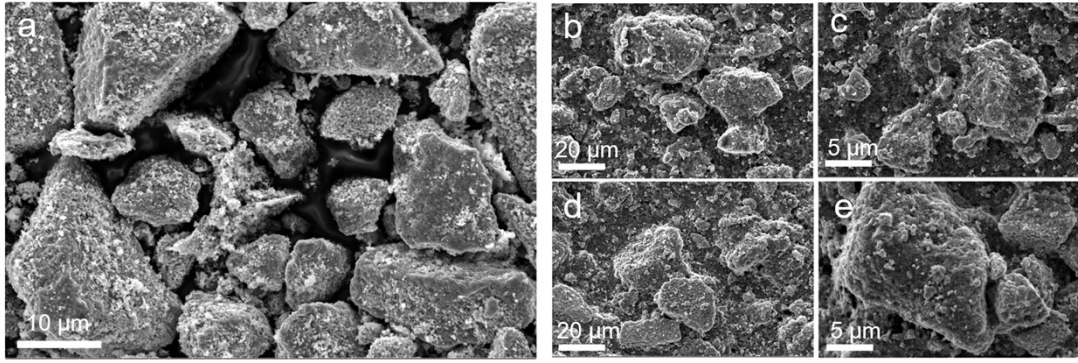
Supplementary Fig.20| Scanning electron microscope images of electrode materials. (a) SEM images of commercial LiMn$_2$O$_4$ material. (b-c) SEM images of LiMn$_2$O$_4$ cathode before cycling. (d-e) Images of LiMn$_2$O$_4$ cathode after 50 cycles at 1 C for Zn|PSE|LiMn$_2$O$_4$ battery.
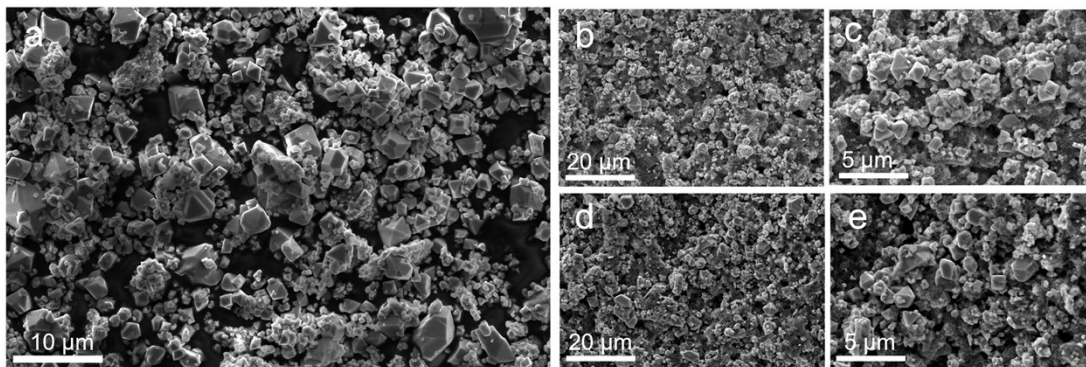
Supplementary Fig.21| Scanning electron microscope images of electrode materials. (a) SEM image of commercial $LiNi_{0.5}Mn_{1.5}O_4$ material. (b-c) SEM images of $LiNi_{0.5}Mn_{1.5}O_4$ cathode before cycling. (d-e) SEM images of $LiNi_{0.5}Mn_{1.5}O_4$ cathode after 50 cycles at 1 C for $Zn|PSE|LiNi_{0.5}Mn_{1.5}O_4$ battery.

Supplementary Fig.22| Scanning electron microscope images of electrode materials. (a) SEM image of as prepared LiCoMnO$_4$ material shows that primary particle connects with each other to form large spheroidal secondary particle. (b-c) SEM images of LiCoMnO$_4$ cathode before cycling. (d-e) SEM images of LiCoMnO$_4$ cathode after 50 cycles at 1 C for Zn|PSE|LiCoMnO$_4$ battery.
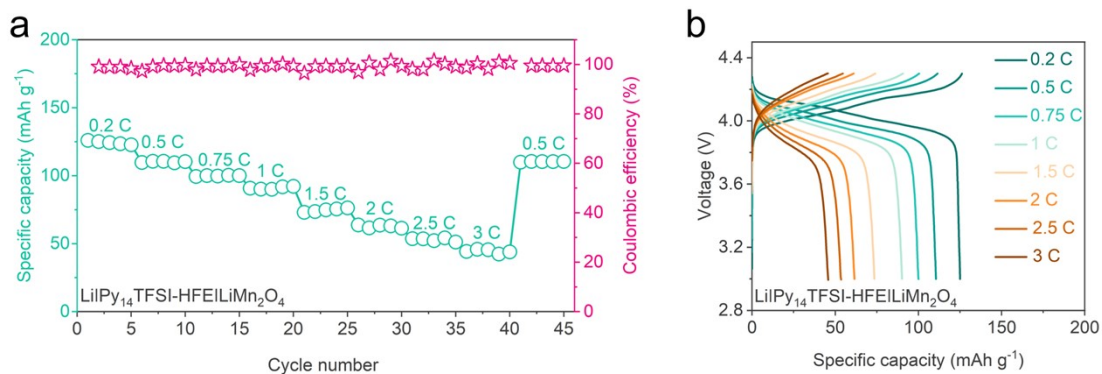
**Supplementary Fig.23| Electrochemical performance of Li|Py$_{14}$TFSI-HFE|LiMn$_2$O$_4$ battery.** (a) The rate performance of LiMn$_2$O$_4$ in Py$_{14}$TFSI-HFE electrolyte using lithium as the anode. (b) Corresponding charge-discharge profiles at different rate.
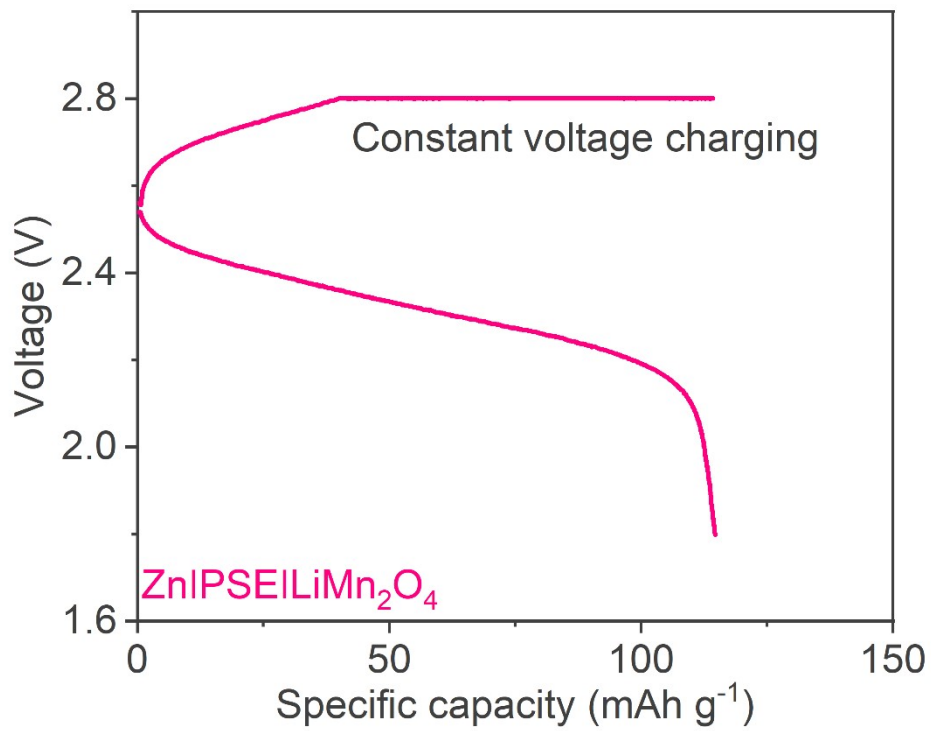
Supplementary Fig.24| The charge-discharge profile of Zn|PSE|LiMn$_2$O$_4$ battery at constant current and constant voltage (CC-CV) mode (3 C galvanostatic charging). The cell delivered a high discharge capacity of 114.7 mAh g^{-1}.
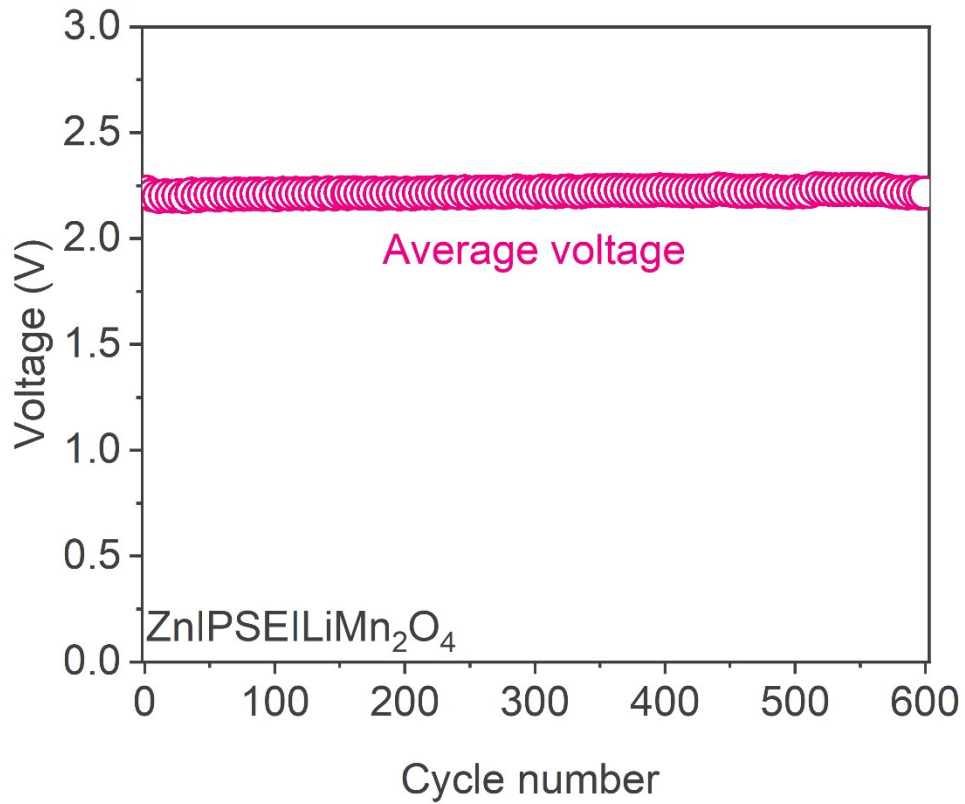
Supplementary Fig.25| The average discharge voltages of Zn|PSE|LiMn$_2$O$_4$ battery at

3 C. The average voltage maintained unchanged over 600 cycles.
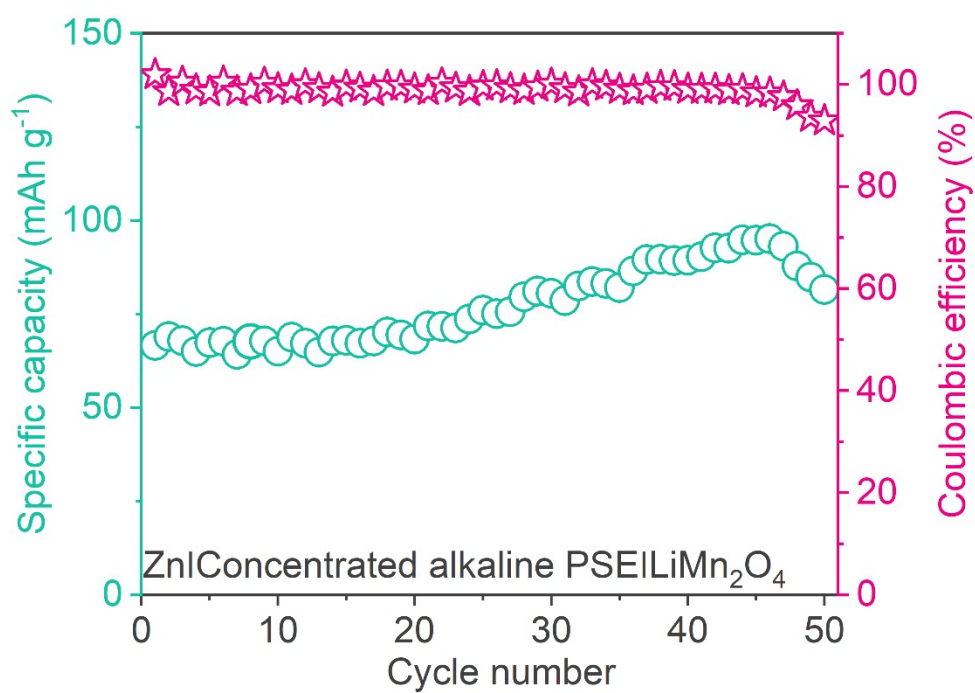
Supplementary Fig.26| The cycling performance of $LiMn_2O_4$ in concentrated alkaline

PSE at 3C.
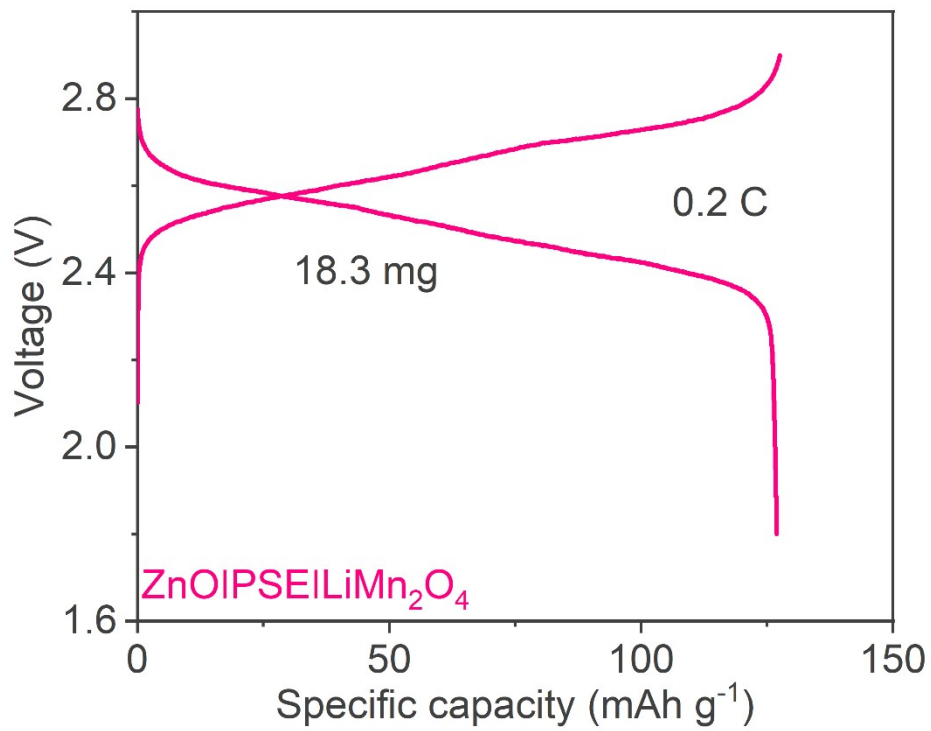
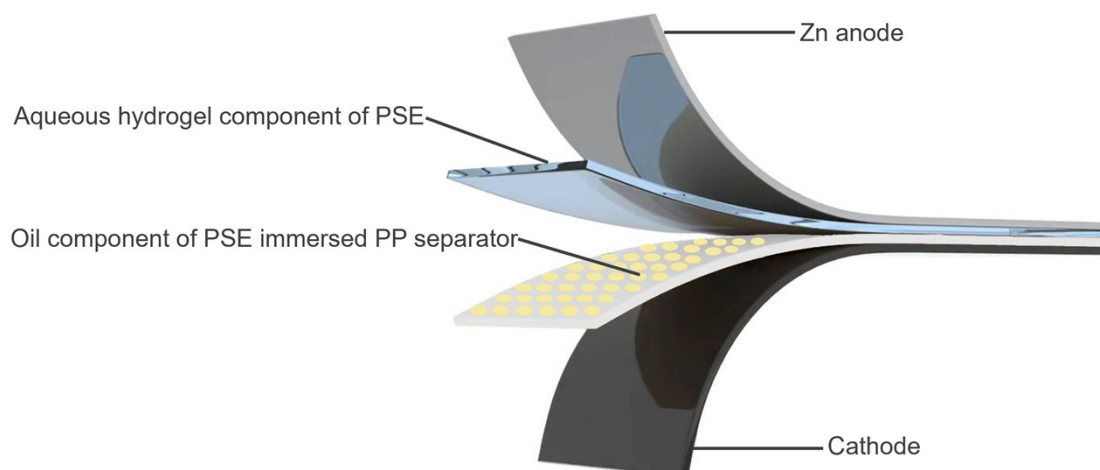**Supplementary Fig.27|** The charge-discharge profile of ZnO|PSE|LiMn$_2$O$_4$ battery with high loading mass of 18.3 mg cm^{-2} at 0.2 C.

Supplementary Fig.28| Schematic of the configuration of the assembled Zn|PSE|LiMn$_2$O$_4$ thin battery based on PSE gel electrolyte. The alkaline gel electrolyte was coated on the anode and the porous PP separator was placed between gel electrolyte and cathode. The aqueous electrolyte was confined in the gel and the porous PP separator was filled with oil-phase organic electrolyte.

Reference

1   Chen, L. *et al.* Achieving High Energy Density through Increasing the Output Voltage: A Highly Reversible 5.3 áV Battery. *Chem* **5**, 896-912 (2019).

2   Frisch, M. J. *et al.* Gaussian 09. *Gaussian 09, Revision D. 01, Gaussian, Inc., Wallingford CT* (2013).

3   Stephens, P. J., Devlin, F. J., Chabalowski, C. F. & Frisch, M. J. Ab-Initio Calculation of Vibrational Absorption and Circular-Dichroism Spectra Using Density-Functional Force-Fields. *J Phys Chem* **98**, 11623-11627, (1994).

4   Kelly, C. P., Cramer, C. J. & Truhlar, D. G. Aqueous solvation free energies of ions and ion-water clusters based on an accurate value for the absolute aqueous solvation free energy of the proton. *J Phys Chem B* **110**, 16066-16081, (2006).

5   Bayly, C. I., Cieplak, P., Cornell, W. & Kollman, P. A. A well-behaved electrostatic potential based method using charge restraints for deriving atomic charges: the RESP model. *J Phys Chem* **97**, 10269 (1993).

6   Zhang, Y. Q. *et al.* Structure and interaction properties of MBIL [Bmim][FeCl4] and methanol: A combined FTIR and simulation study. *J Mol Liq* **309**, (2020).

7   Jorgensen, W. L., Maxwell, D. S. & TiradoRives, J. Development and testing of the OPLS all-atom force field on conformational energetics and properties of organic liquids. *J Am Chem Soc* **118**, 11225-11236, (1996).

8   Bussi, G., Donadio, D. & Parrinello, M. Canonical sampling through velocity rescaling. *J Chem Phys* **126**, 014101 (2007).

9   Parrinello, M. & Rahman, A. Polymorphic transitions in single crystals: A new

molecular dynamics method. *J Appl Phys* **52**, 7182 (1981).

10   Darden, T., York, D. & Pedersen, L. Particle mesh Ewald: An N·log(N) method for Ewald sums in large systems. *J Chem Phys* **98**, 10089 (1993).

11   Hess, B., Bekker, H., Berendsen, H. J. C. & Fraaije, J. G. E. M. LINCS: A linear constraint solver for molecular simulations. *J Comput Chem* **18**, 1463 (1997).

12   Shin, H. C. *et al.* Asymmetry between charge and discharge during high rate cycling in LiFePO4–In Situ X-ray diffraction study. *Electrochemistry Communications* **10**, 536-540 (2008).

13   Wang, Y., He, P. & Zhou, H. Olivine LiFePO 4: development and future. *Energy & Environmental Science* **4**, 805-817 (2011).

14   Bak, S.-M., Shadike, Z., Lin, R., Yu, X. & Yang, X.-Q. In situ/operando synchrotron-based X-ray techniques for lithium-ion battery research. *NPG Asia Materials* **10**, 563-580 (2018).

15   Alcantara, R., Jaraba, M., Lavela, P. & Tirado, J. X-ray diffraction and electrochemical impedance spectroscopy study of zinc coated LiNi0. 5Mn1. 5O4 electrodes. *Journal of Electroanalytical Chemistry* **566**, 187-192 (2004).

16   Wang, L., Li, H., Huang, X. & Baudrin, E. A comparative study of Fd-3m and P4332 "LiNi0. 5Mn1. 5O4". *Solid State Ionics* **193**, 32-38 (2011).

17   Liu, S., He, H. & Chang, C. Understanding the improvement of fluorination in 5.3 V LiCoMnO4 spinel. *Journal of Alloys and Compounds* **860**, 158468 (2021).

18   Ariyoshi, K., Yamamoto, H. & Yamada, Y. High dimensional stability of

LiCoMnO4 as positive electrodes operating at high voltage for lithium-ion batteries with a long cycle life. *Electrochimica Acta* **260**, 498-503 (2018).

19   Chen, L. *et al.* Achieving high energy density through increasing the output voltage: a highly reversible 5.3 V battery. *Chem* **5**, 896-912 (2019).